

Quantum dots and tunnel barriers in InAs/InP nanowire heterostructures: Electronic and optical properties

Yann-Michel Niquet* and Dulce Camacho Mojica

Institute for Nanosciences and Cryogenics (INAC), SP2M/L_Sim, CEA Grenoble, 38054 Grenoble Cedex 9, France

(Received 24 September 2007; revised manuscript received 1 February 2008; published 12 March 2008)

We compute the structural and electronic properties of $\langle 111 \rangle$ -oriented InAs/InP nanowire heterostructures using Keating's valence force field and a tight-binding model. We focus on the optical properties (exciton energies and polarization) of InAs quantum dots embedded in InP nanowires and on the height of InP and InAsP tunnel barriers embedded in InAs nanowires. We show that InAs quantum dots exhibit bright optical transitions, at variance with the highly mismatched InAs/GaAs nanowire heterostructures. The polarization of the photons is perpendicular to the nanowire for thin InAs layers but rotates parallel to the nanowire for thick enough ones, as a result of the increasing light-hole character of the exciton. As for tunnel barriers, we show that the residual strains can significantly reduce the conduction band discontinuity in thin InAsP layers. This must be taken into account in the design of nanowire tunneling devices.

DOI: [10.1103/PhysRevB.77.115316](https://doi.org/10.1103/PhysRevB.77.115316)

PACS number(s): 73.21.Hb, 78.67.Lt, 73.43.Cd

I. INTRODUCTION

The recent breakthroughs made in the catalytic growth of semiconductor nanowires¹⁻³ have allowed the synthesis of high-quality heterostructures with outstanding optical and transport properties.⁴ The composition of the nanowires can actually be modulated along the growth axis⁵⁻⁷ (axial heterostructures), as well as radially⁸ (core-shell structures). Nanowire heterostructures are very attractive because they can accommodate much larger misfit strains than quantum well heterostructures.^{9,10} They are, indeed, able to relax very efficiently by distorting the surface of the nanowire.¹¹ The critical thickness h_c for plastic strain relaxation is therefore expected to increase with decreasing wire diameter and to eventually become infinite below some critical radius R_c depending on the materials. This would allow the epitaxial growth of arbitrary and unprecedented heterostructures. As a matter of fact, various Si/Ge (Refs. 7, 8, 12, and 13) and III-V (Refs. 14-16) nanowire heterostructures have now been successfully synthesized and appear to be promising building blocks for future nanoelectronics.¹⁷ The InAs/InP system has, in particular, attracted much attention.^{6,18-21} Resonant tunneling diodes,²² field-effect transistors,²³ Coulomb blockade devices,²⁴⁻²⁶ and quantum dot memories^{27,28} for example, have been realized with InAs nanowires split by InP tunnel barriers. Light emission has also been demonstrated from single InAsP quantum dots (QDs) embedded in doped InP nanowires (nanowire light-emitting diodes).²⁹

The residual strains in nanowire heterostructures might, however, have a significant impact on their electronic and optical properties. In Refs. 30 and 31, we have investigated the case of InAs/GaAs nanowire heterostructures (NWHETs) and core-shell structures as the prototypes of highly mismatched systems (lattice mismatch $\varepsilon_{||} = -6.69\%$). We have shown that the strains and piezoelectric fields could be large enough to separate the electrons from the holes in the InAs layers, which strongly reduces the oscillator strength of the excitons. In this paper, we compute the structural and electronic properties of the more widespread InAs/InP NWHETs ($\varepsilon_{||} = -3.13\%$). We show that the strains,

though still having sizeable effects, do not alter the *qualitative* behavior of these heterostructures [when compared to unstrained systems such as GaAs/AlAs (Refs. 32 and 33)]. As a consequence, the InAs quantum dots exhibit bright optical transitions. This is consistent with the experimental results, the spectroscopy of InAs/InP nanowires^{21,29} being more successful than the spectroscopy of InAs/GaAs NWHETs^{34,35} up to now. Interestingly, the luminescence of InAs/InP NWHETs is polarized perpendicular to the nanowire for thin InAs layers but parallel to the nanowire for thick ones, as a result of the increasing light-hole character of the exciton. We have also computed the height of InP and InAsP tunnel barriers embedded in InAs nanowires.³⁶ We show that the strains can significantly reduce the conduction band discontinuity in thin layers, which might increase, e.g., the leakage through InAs/InP nanowire memory elements.^{27,28}

The paper is organized as follows: The computational methods are briefly reviewed in Sec. II; then, the optical properties of InAs QDs in InP nanowires are discussed in Sec. III; the height of InAsP barriers in InAs nanowires is finally discussed in Sec. IV.

II. NANOWIRE STRUCTURES AND METHODOLOGY

We consider $\langle 111 \rangle$ -oriented, cylindrical InAs/InP nanowires with the zinc-blende structure. They are characterized by their radius R and by the thicknesses t_{InAs} and t_{InP} of the InAs and InP layers, respectively (periodic boundary conditions being applied along the nanowire axis). The optical properties of InAs quantum dots in InP nanowires were, on one hand, investigated in the range $4 \leq t_{\text{InAs}} \leq 16$ nm and for $R = 10-16$ nm. The period of the heterostructure, $L = t_{\text{InAs}} + t_{\text{InP}} \approx 40$ nm, was chosen long enough to avoid significant elastic or electronic interactions between the dots. The heights of InP barriers in InAs nanowires were, on the other hand, computed in the range $2 \leq t_{\text{InP}} \leq 96$ nm and for $R = 10-30$ nm. The dangling bonds at the surface of the nanowires are saturated with hydrogen atoms. The reference frame is $x = [1\bar{1}0]$, $y = [11\bar{2}]$, and $z = [111]$.

The methods used to compute the structural and electronic properties of these nanowires have been discussed in detail in Ref. 30. The strain distribution and actual period L of the heterostructures are calculated with Keating's valence force field (VFF) model.³⁷ In this atomistic approach, each material is characterized by a "bond-stretching" and a "bond-bending" elastic constant, which are fitted³⁸ to the bulk modulus and Poisson ratio ν_{111} . The strains displace the anions with respect to the cations, which give rise to a piezoelectric field in the heterostructure. The piezoelectric polarization density $\mathbf{P} = 2e_{14}(\varepsilon_{y'z'}, \varepsilon_{x'z'}, \varepsilon_{x'y'})$ is, to first order, proportional to the shear strains in the cubic axis set $\{x' = [100], y' = [010], z' = [001]\}$ [$e_{14} = -0.045$ C/m² in InAs and $e_{14} = -0.035$ C/m² in InP (Ref. 39)]. Poisson's equation for the piezoelectric potential is solved with a finite difference method.⁴⁰

The one-particle electronic structure of the InAs QDs is computed with a $sp^3d^5s^*$ tight-binding⁴¹⁻⁴³ (TB) model based on the parametrization of Jancu *et al.*⁴⁴ Onsite couplings between the p and between the d orbitals have been added to reproduce the conduction and valence band deformation potentials.^{45,46} Spin-orbit coupling and self-energy (image charge) corrections are taken into account. The latter arise from the dielectric mismatch between the nanowires (with dielectric constant κ_{in}) and their surroundings (with dielectric constant κ_{out}) and have been discussed in detail in Refs. 30 and 47. Unless otherwise stated, we assume $\kappa_{out} = 1$ (vacuum).⁴⁸ The eigenstates of the supercell (1 333 280 atoms for $R = 16$ nm and $L \approx 40$ nm) are computed with a preconditioned Jacobi-Davidson algorithm.^{47,49}

The exciton energies are last calculated assuming uncorrelated electron-hole pairs (strong confinement regime). The electron wave function ψ_e is optimized in the average potential V_h created by the hole, while the hole wave function ψ_h is optimized in the average potential V_e created by the electron. The electrostatic potentials V_e and V_h are again computed with a finite difference method.

III. InAs QUANTUM DOTS IN InP NANOWIRES

In this section, we discuss the strains and piezoelectric fields in InAs quantum dots embedded in InP nanowires (Sec. III A), and their electronic and optical properties (Secs. III B and III C). The similarities and differences with the highly mismatched InAs/GaAs NWHTs^{30,31} are outlined.

A. Strain relaxation and piezoelectric fields

The InAs layers, which tend to be compressed by the majority material (InP), can relax strains by expanding outward, thereby distorting the surface of the nanowire. They transfer tensile strains that way to the InP layers around the interfaces. The *normalized* strain distributions $\varepsilon_{ij}/\varepsilon_{\parallel}$ (where ε_{\parallel} is the lattice mismatch) actually look quite close in InAs/InP and InAs/GaAs heterostructures.^{30,31} They are, in particular, very inhomogeneous in thin InAs layers, the axis of the nanowire being still significantly compressed, while its surface is (over-)relaxed. The strains in thick InAs layers are

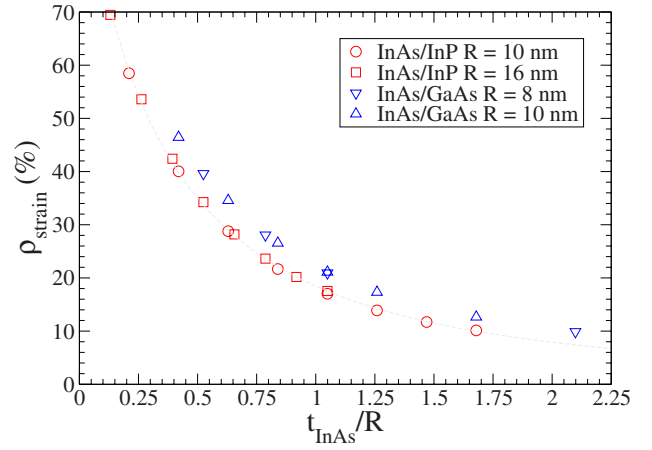


FIG. 1. (Color online) The strain ratio ρ_{strain} as a function of t_{InAs}/R in InAs/GaAs and InAs/InP nanowire heterostructures. The dashed line is Eq. (2).

much more homogeneous, noticeable only near the interfaces.

The residual strains in the InAs QDs can be characterized by the average hydrostatic deformation $\Delta\Omega/\Omega_0 = (\Omega - \Omega_0)/\Omega_0$, where Ω and Ω_0 are, respectively, the actual and unstrained volumes of the InAs layer. It would be $(\Delta\Omega/\Omega_0)_{\text{QW}} = -4.50\%$ in an InAs/InP quantum well (QW) biaxially strained to a $\langle 111 \rangle$ -oriented InP buffer.⁵⁰ For the sake of comparison with InAs/GaAs heterostructures [$(\Delta\Omega/\Omega_0)_{\text{QW}} = -9.56\%$], we can define a normalized average strain in the InAs layer,⁵¹

$$\rho_{\text{strain}} = \frac{\Delta\Omega}{\Omega_0} \bigg/ \left(\frac{\Delta\Omega}{\Omega_0} \right)_{\text{QW}}. \quad (1)$$

The strain ratio ρ_{strain} would be 100% in a QW ($R \rightarrow \infty$) and 0 in a fully relaxed NWHT, and would only depend on t_{InAs}/R in a linear elasticity approximation⁵² (at least in the $L \rightarrow \infty$ limit). It is plotted in Fig. 1 for InAs/InP and InAs/GaAs NWHTs with different radii.⁵³ As expected, ρ_{strain} rapidly decreases with increasing t_{InAs}/R , being only $\approx 50\%$ for $t_{\text{InAs}} = R/4$. InAs/InP and InAs/GaAs heterostructures, moreover, follow the same trends, although the InAs layers are slightly more relaxed in InP than in GaAs. The elastic constants of InP are, as a matter of fact, smaller than those of GaAs. The small deviations from the expected t_{InAs}/R dependence arise from nonlinearities in Keating's VFF model and from finite L effects. In InAs/InP heterostructures, ρ_{strain} can be fitted (for $0 \leq t_{\text{InAs}}/R \leq 2$) by

$$\rho_{\text{strain}} = \frac{1}{1 + 3.01(t_{\text{InAs}}/R) + 1.41(t_{\text{InAs}}/R)^2}, \quad (2)$$

which is plotted as a dashed line in Fig. 1.

The piezoelectric potential induced by these strains is plotted in Fig. 2 along the axis of InAs/InP NWHTs with radius $R = 10$ nm. As discussed in Ref. 30, the piezoelectric polarization density $\mathbf{P} = P_z \mathbf{z} = (2e_{14}/\sqrt{3})(\varepsilon_{zz} - \varepsilon_{\parallel})\mathbf{z}$ is nonzero even in biaxially strained, $\langle 111 \rangle$ -oriented InAs QWs. Such a homogeneous polarization is equivalent to a transfer of sur-

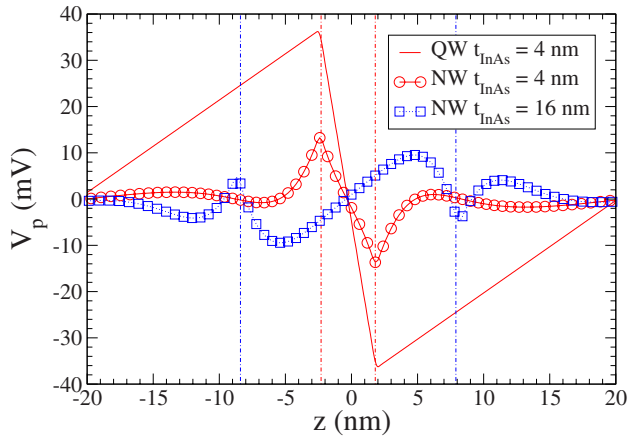


FIG. 2. (Color online) The piezoelectric potential in an InAs/InP quantum well ($t_{\text{InAs}}=4$ nm) and along the axis of InAs/InP nanowire (NW) heterostructures ($R=10$ nm, $t_{\text{InAs}}=4$ and 16 nm). The vertical dash-dotted lines delimit the InAs layers.

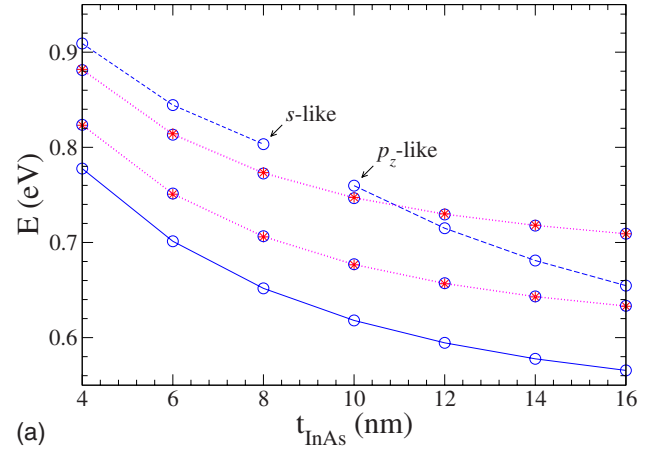
face charges $\sigma = \pm P_z$ from one interface to another,⁵⁴ making the InAs QWs look like parallel plate capacitors. Thin InAs layers embedded in InP nanowires still behave like parallel plate capacitors, the electric field being almost uniform along the axis of the nanowire, as evidenced in Fig. 2. The magnitude of the electric field in the 4 nm thick layers, $E_z \approx 6.73$ MV/m, is, however, much smaller than in the equivalent QW, $E_z = 17.1$ MV/m, due to strain relaxation and finite-size effects. At variance with QWs, the piezoelectric polarization density is also sizeable in InP close to the interfaces. The polarizations in InAs and InP have, however, opposite directions; the piezoelectric field therefore decreases rapidly in the InP layers that screen the InAs QDs.

The structure of the piezoelectric field is much more complex in thick InAs layers. The piezoelectric polarization density indeed remains significant only near the InAs/InP interfaces. Therefore, the 16 nm thick InAs layer behaves (in a first, very crude approximation) as $two \approx 4$ nm thick parallel plate capacitors in series (one on the inner side of each interface). This notably results in a reversal of the piezoelectric field at the center of the QD (see Fig. 2).

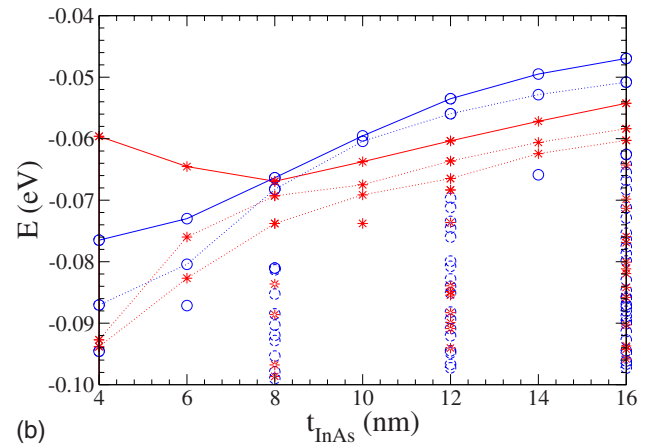
In average, the piezoelectric field is much smaller in InAs/InP than in InAs/GaAs NWHETs.³⁰ This is mostly due to the lower lattice mismatch between InAs and InP and to the smaller piezoelectric constant of InP. The maximum difference of potential across the InAs layers hardly exceeds $\Delta V_p = 40$ meV for $R=10$ nm (instead of $\Delta V_p \approx 300$ meV in InAs/GaAs NWHETs⁵⁵). It, however, reaches $\Delta V_p \approx 70$ meV for $R=16$ nm due to reduced finite-size effects (larger cross-sectional area). The second-order model of Ref. 56 for the piezoelectric polarization density (whose parameters are, however, only known for InAs) yields slightly higher ΔV_p 's. The impact of strains and piezoelectric fields on the electronic structure of the NWHETs will be discussed in the next paragraph.

B. Electronic structure

The lowest single-electron and single-hole energies in InAs/InP NWHETs with radius $R=10$ nm are plotted as a



(a)



(b)

FIG. 3. (Color online) Single-electron (a) and single-hole (b) energies in InAs/InP nanowire heterostructures with radius $R=10$ nm. Circles (stars) are single-particle states with symmetry $E_{1/2}$ ($E_{3/2}$). The lines are just guides to the eyes. The valence band structure down to $E \approx -0.1$ eV has been computed for $t_{\text{InAs}}=4, 8, 12,$ and 16 nm.

function of t_{InAs} in Fig. 3. The reference of energies is the valence band edge of bulk, unstrained InAs. The single-particle states have been sorted into the irreducible representations $E_{1/2}$ (circles) and $E_{3/2}$ (stars) of the double group (C_{3v}) of the nanowire. They are all twofold (spin) degenerate. The squared envelopes of selected electron (E_i) and hole (H_i) wave functions are plotted in Figs. 4 and 5.⁵⁷

Let us discuss the single-electron levels first. The ground state, E_1 , exhibits a clear s -like wave function. Its energy rises from $E=0.566$ eV for $t_{\text{InAs}}=16$ nm to $E=0.778$ eV for $t_{\text{InAs}}=4$ nm due to the increase of quantum confinement and strains (see discussion below). It is well separated from the nearly degenerate E_2 and E_3 levels. The E_2 and E_3 wave functions are (mainly) linear combinations of p_x - and p_y -like envelopes.⁵⁸ The splitting between E_1 and E_2/E_3 essentially depends on R (and not much on t_{InAs}) since these states mostly differ by their radial behavior. In thin InAs layers ($t_{\text{InAs}} \leq 10$ nm), the nearly degenerate E_4 and E_5 states are linear combinations of $d_{x^2-y^2}$ - and d_{xy} -like envelopes, while E_6 is again s -like. In thicker InAs layers, however, E_4 is a

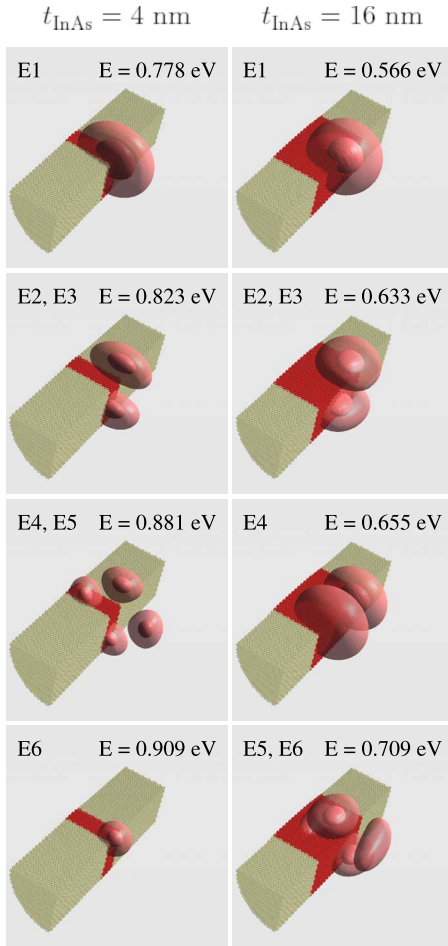


FIG. 4. (Color online) Isoprobability surfaces of selected electron wave functions in InAs/InP nanowire heterostructures ($R=10$ nm, $t_{\text{InAs}}=4$ and 16 nm) (Refs. 57 and 58). Only one quarter of the nanowire is shown for clarity. As atoms appear in dark gray (in red in the color online figure).

p_z -like state that will ultimately cross the $p_{x,y}$ -like levels E2 and E3 (when $t_{\text{InAs}} \geq 20$ nm), as lateral confinement by the nanowire becomes stronger than longitudinal confinement by the heterostructure.

As discussed in Refs. 30 and 31, compressive strains tend to rise the conduction band of InAs and make a significant

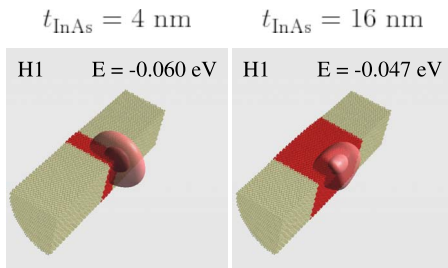


FIG. 5. (Color online) Isoprobability surfaces of the ground-state hole wave function in InAs/InP nanowire heterostructures ($R=10$ nm, $t_{\text{InAs}}=4$ and 16 nm). Only one quarter of the nanowire is shown for clarity. As atoms appear in dark gray (in red in the color online figure).

contribution to the opening of the band gap in thin, weakly relaxed layers. This is evidenced in Table I, which gives the contributions of strains, piezoelectric fields, and self-energy corrections to the E1 (and H1) energies. As expected, the strain-induced shifts Δ_s are much lower in InAs/InP than in the highly mismatched InAs/GaAs NWHETs (see Ref. 30 for a comparison). More importantly, the inhomogeneous strain distribution in thin InAs layers was shown to dig a well at the surface of the nanowires. This well is actually able to trap the electrons in InAs/GaAs NWHETs, which is not desirable for most practical applications. Figure 4 shows that this is not the case in InAs/InP heterostructures. The strain-induced surface well is, as a matter of fact, about twice less deep in InAs/InP than in InAs/GaAs heterostructures. The above conclusions also hold when the self-energy corrections, which tend to repel the electrons from the surface,^{30,47} are zero (i.e., when $\kappa_{\text{in}} = \kappa_{\text{out}}$) and at least up to $R=20$ nm. The electrons are, however, very light in InAs ($m^*=0.023m_0$) and, therefore, a little sensitive to the strain-induced potential. They might be trapped by the strains even at a moderate lattice mismatch in other materials with larger effective masses.

The hole level structure is more intricate. The density of states is much larger on the valence band side (and rapidly increases with R), as shown in Fig. 3(b). There is, interestingly, a crossover (around $t_{\text{InAs}} \approx 8$ nm for $R=10$ nm and around $t_{\text{InAs}} \approx 11$ nm for $R=16$ nm) between a ground state with symmetry $E_{3/2}$ and a ground state with symmetry $E_{1/2}$. This crossover is driven by the increasing light-hole character of H1, which is a heavy-hole state in thin InAs layers but an almost light-hole state in homogeneous InAs nanowires. This is evidenced in Table II, which gives the heavy- and light-hole band contributions to H1 as a function of t_{InAs} .⁵⁹ As discussed in the next paragraph, this crossover between the $E_{3/2}$ and $E_{1/2}$ symmetries has important consequences on the strength and polarization of the optical transitions. It results from strain relaxation and from the balance between lateral and longitudinal confinements. Indeed, compressive strains and longitudinal confinement by the heterostructure tend to favor a heavy-hole ground state in thin InAs layers (like in quantum wells⁶⁰). However, their influence decreases with respect to lateral confinement when increasing t_{InAs} . The hole therefore tends to get heavier along x and y (which become the main directions of confinement), and thus lighter along $[111]$ [since heavy holes along x and y are mostly light along z (Ref. 61)]. The increase of the light-hole character of H1 is also reflected in the spread of the wave functions in Fig. 5. The above trends should be qualitatively (if not quantitatively) valid in the hexagonal phase⁶² (commonly encountered in III-V nanowires⁶³), provided that the crystal field splitting in bulk wurtzite InAs is not too large with respect to the confinement energies.

The overall behavior of the holes is very different in InAs/GaAs and InAs/InP NWHETs. In particular, the piezoelectric field is large enough in InAs/GaAs nanowires to separate the holes from the electrons and to squeeze the former against one of the interfaces.³⁰ At variance, the holes seem a little sensitive to the (much weaker) piezoelectric field in InAs/InP heterostructures. This is evidenced by the low expectation values of the piezoelectric potential ($\langle V_p \rangle$)

TABLE I. Energy (E), strain-induced shift (Δ_s), expectation value of the piezoelectric potential ($\langle V_p \rangle$), and self-energy correction ($\pm \langle \Sigma \rangle$) as a function of t_{InAs} and R for the lowest-lying hole (H1) and electron (E1) state (Ref. 57).

R (nm)	t_{InAs} (nm)		E (eV)	Δ_s (meV)	$\langle V_p \rangle$ (meV)	$\pm \langle \Sigma \rangle$ (meV)
10.0	4.0	H1	-0.060	12.1	0.9	-37.5
		E1	0.778	89.6	-1.3	41.0
	16.0	H1	-0.047	6.5	0.9	-35.9
		E1	0.566	18.0	-1.0	40.9
16.0	4.0	H1	-0.018	24.8	3.4	-22.5
		E1	0.764	108.8	-2.9	26.2
	16.0	H1	-0.027	11.2	5.3	-25.9
		E1	0.545	39.7	-0.9	25.9

given in Table I. The effects of the piezoelectric field are somewhat stronger, though, at larger R 's due to the increase of strains and decrease of finite-size effects discussed in Sec. III A.

C. Optical properties

In this paragraph, we discuss the optical properties (exciton energies, oscillator strengths and luminescence polarization) of InAs/InP NWHETs.

The exciton energy E_0 is plotted as a function of t_{InAs} in Fig. 6. Data for InAs/InP NWHETs with radius $R=10$ nm and $R=16$ nm and for InAs/GaAs NWHETs with radius $R=10$ nm are shown.³⁰ As expected, the exciton energy, which follows the trends of the E1 level, steadily decreases with t_{InAs} . The optical band gaps of InAs/InP NWHETs with radius $R=10$ nm and $R=16$ nm are surprisingly close. This results from various cancellations between the different contributions to E_0 : The decrease of the confinement energy with increasing R is partly compensated by the enhancement of the strain shifts Δ_s (see Table I), while the decrease of the self-energy corrections is compensated by a decrease of the exciton Coulomb energy W (see discussion below). The optical band gap is, on the other hand, lower in InAs/InP than in InAs/GaAs NWHETs, at least for thin InAs layers. This is due to the larger lattice mismatch and (unstrained) conduction band offset in the latter system.

TABLE II. Heavy-hole (HH) and light-hole (LH) band contributions to the H1 wave function as a function of t_{InAs} (the axis of quantization being $z=[111]$). The $t_{\text{InAs}} \rightarrow \infty$ data correspond to a homogeneous InAs nanowire with the same radius $R=10$ nm.

t_{InAs} (nm)	$E(\text{H1})$ (eV)	HH (%)	LH (%)
4.0	-0.060	93.9	2.5
8.0	-0.066	56.4	41.1
16.0	-0.047	31.2	67.4
∞	-0.045	16.4	83.0

The exciton Coulomb energy $W = e \langle \psi_e | V_h | \psi_e \rangle = -e \langle \psi_h | V_e | \psi_h \rangle$ is plotted in the inset of Fig. 6. As discussed in Ref. 30, W is dominated by the image charge contributions (interaction of the electron with the image charges of the hole and vice-versa), at least when $\kappa_{\text{in}} \gg \kappa_{\text{out}}$. It therefore cancels the self-energy corrections, the net effect of the Coulomb interactions (self-energy plus exciton) being a decrease of one-particle band gap by a few meV. W behaves as $1/R$ but depends very little on t_{InAs} (like the self-energy corrections). Moreover, the self-consistent calculations show that the electron-hole interaction does not mix the single-particle states very much in the investigated range of dimensions. From now on, we will therefore approximate the energy of the optical transition between the single-particle states H_i and E_j by $E_{ij} = E(E_j) - E(H_i) - W_{ij}$, where $W_{ij} = e \langle E_j | V_h[H_i] | E_j \rangle$ and $V_h[H_i]$ is the average potential created by the hole.

In practice, the InAs layer is often alloyed with phosphorus. To investigate the effects of alloying on the optical properties of NWHETs, we have simulated InAs_{0.5}P_{0.5} quan-

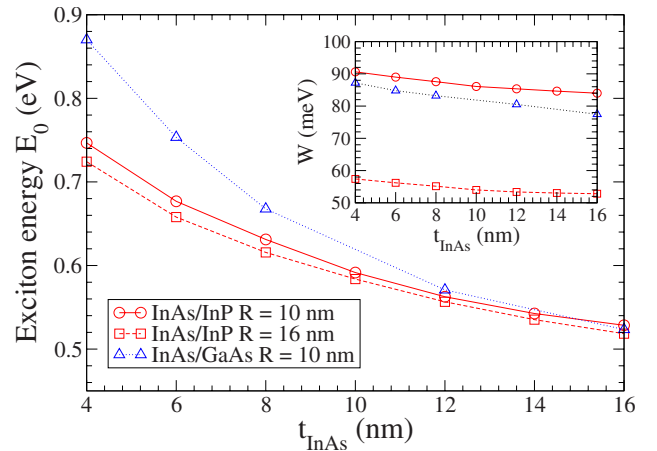


FIG. 6. (Color online) Exciton energies E_0 in InAs/InP nano-wire heterostructures with radii $R=10$ and $R=16$ nm and in InAs/GaAs heterostructures with radius $R=10$ nm. Inset: exciton Coulomb energies W .

tum dots embedded in InP nanowires ($R=10$ nm) using a random distribution of As and P atoms. The optical band gap of such nanowires ranges from $E_0=1.106$ eV for $t_{\text{InAs}}=4$ nm to $E_0=0.979$ eV for $t_{\text{InAs}}=16$ nm, i.e., $\approx 350\text{--}450$ meV above the optical band gap of pure InAs quantum dots. This follows from an increase of the band gap energy of the bulk material [$E_g(\text{InAs}_{0.5}\text{P}_{0.5})\approx 0.91$ eV while $E_g(\text{InAs})=0.418$ eV] and from a decrease of strains and quantum confinement. The exciton binding energy W is little affected by alloying.

We will now discuss the polarization of the light emitted by the NWHETs. In the electric dipole approximation, the rate of absorption or emission between the single-particle states H_i and E_j can be characterized by the dimensionless oscillator strength,^{43,61,64}

$$f_{ij}(\mathbf{e}) = \frac{2}{m_0} \frac{|\langle E_j | \mathbf{e} \cdot \mathbf{p} | H_i \rangle|^2}{E_{ij}}, \quad (3)$$

where \mathbf{p} is the momentum operator and \mathbf{e} is the polarization (direction of the electric field) of the photon with energy E_{ij} (and wavelength $\lambda_{ij}=hc/E_{ij}\gg R$). We focus on parallel and perpendicular polarizations⁶⁵ and, therefore, define f_{ij}^{\parallel} and f_{ij}^{\perp} and $f_{ij}^{\perp}=f_{ij}(\mathbf{x})\approx f_{ij}(\mathbf{y})$. f_{ij}^{\perp} and f_{ij}^{\parallel} account for the *intrinsic* sources of polarization anisotropy (i.e., band structure and symmetry related). In particular, parallel-polarized transitions are allowed only between states with the same symmetry ($E_{1/2}$ or $E_{3/2}$), while perpendicular-polarized transitions are forbidden between the $E_{3/2}$ states. There is, in addition, an *extrinsic* source of polarization anisotropy: The far field \mathbf{E}_{out} outside the nanowire might indeed differ from the electric field $\mathbf{E}_{\text{in}}=K\mathbf{E}_{\text{out}}$ inside the nanowire due to the dielectric mismatch with the environment (local-field effects).^{66–69} Namely,

$K_{\parallel}=1$ in the \parallel polarization,

$$K_{\perp} = \frac{2\kappa_{\text{out}}}{\kappa_{\text{in}} + \kappa_{\text{out}}} \text{ in the } \perp \text{ polarization.} \quad (4)$$

The *effective* parallel and perpendicular oscillator strengths are therefore

$$\begin{aligned} F_{ij}^{\parallel} &= K_{\parallel}^2 f_{ij}^{\parallel} = f_{ij}^{\parallel}, \\ F_{ij}^{\perp} &= K_{\perp}^2 f_{ij}^{\perp}. \end{aligned} \quad (5)$$

The bare oscillator strength f_{ij}^{\perp} is thus heavily reduced by local-field effects (LFEs) in vacuum or air ($K_{\perp}^2=1/42.25$ for $\kappa_{\text{in}}=12$ and $\kappa_{\text{out}}=1$).

For a given polarization, the average radiative recombination rate at temperature T can finally be written as⁷⁰

$$\langle \omega \rangle \propto K^2 \frac{\sum_{i,j} E_{ij}^2 f_{ij} e^{-E_{ij}/(kT)}}{\sum_{i,j} e^{-E_{ij}/(kT)}}. \quad (6)$$

The polarization anisotropy will be characterized by the linear polarization ratio,

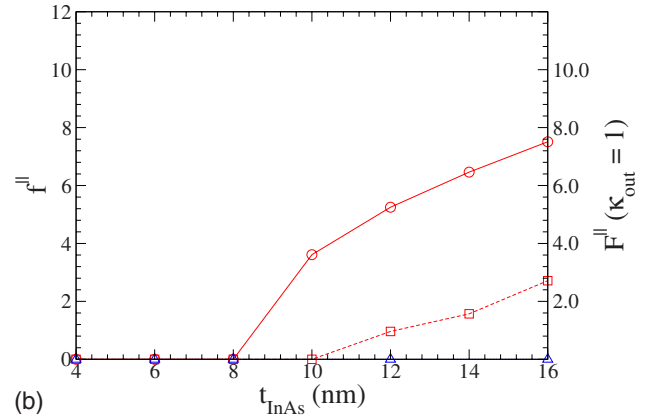
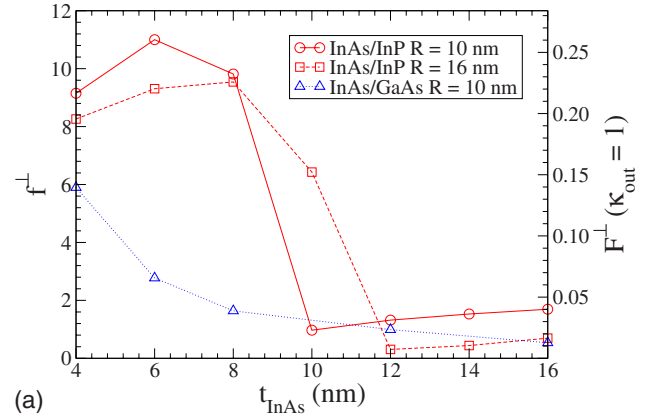


FIG. 7. (Color online) Perpendicular (a) and parallel (b) E1H1 oscillator strengths in InAs/InP nanowire heterostructures with radii $R=10$ and $R=16$ nm and in InAs/GaAs heterostructures with radius $R=10$ nm.

$$\rho_{\text{pola}} = \frac{\langle \omega_{\parallel} \rangle - \langle \omega_{\perp} \rangle}{\langle \omega_{\parallel} \rangle + \langle \omega_{\perp} \rangle}, \quad (7)$$

which is +1 (−1) when the light is fully parallel polarized (perpendicular polarized). The matrix elements of the momentum operator \mathbf{p} are computed along the lines of Ref. 71.

The bare (f_{11}) and effective (F_{11}) E1H1 oscillator strengths are plotted in Fig. 7 for the same nanowires, as in Fig. 6. The photons emitted by this transition are clearly polarized perpendicular to the nanowire in thin InAs layers. Indeed, as discussed in the previous paragraph, the hole ground state has the $E_{3/2}$ symmetry when $t_{\text{InAs}}\lesssim 8$ nm ($R=10$ nm) or $t_{\text{InAs}}\lesssim 11$ nm ($R=16$ nm), while the electron ground state always has the $E_{1/2}$ symmetry. The parallel polarization is therefore symmetry forbidden in these ranges.⁷² The effective oscillator strength F_{11}^{\perp} is, nonetheless, rather weak in vacuum or air due to local-field effects. All polarizations become, at variance, allowed beyond the crossover between the $E_{3/2}$ and $E_{1/2}$ hole ground states. The heavy-hole part of the H1 wave function does not, however, contribute to f_{11}^{\perp} nor to f_{11}^{\parallel} in the $E_{1/2}$ symmetry.⁷³ As a consequence, $f_{11}^{\parallel} \approx 4f_{11}^{\perp}$, as expected for pure light-hole transitions ($\rho_{\text{pola}} \rightarrow 0.6$ at $T=0$ K without LFEs).^{61,67} The parallel oscillator

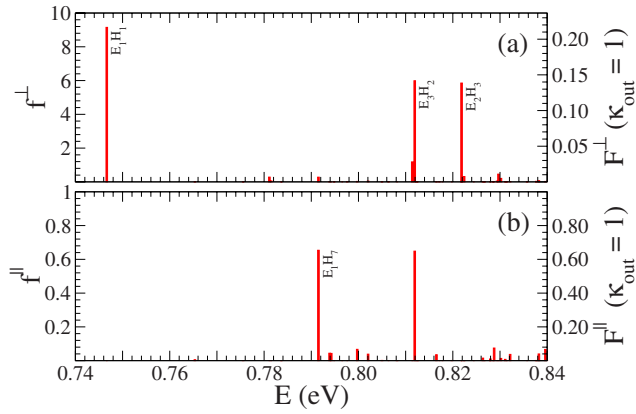


FIG. 8. (Color online) Oscillator strength spectrum (parallel and perpendicular polarizations) of InAs/InP nanowire heterostructures with $R=10$ nm and $t_{\text{InAs}}=4$ nm.

strength is much smaller for $R=16$ nm than for $R=10$ nm, as a result of the larger piezoelectric fields that tend to separate the electron from the hole—although not as much as in InAs/GaAs NWHETs.³⁰ In the latter case, the E1H1 transition remains polarized perpendicular to the nanowire because the piezoelectric field, which flattens the hole against one of the interfaces, prevents the $E_{3/2}$ to $E_{1/2}$ crossover evidenced in InAs/InP NWHETs. InAs_{0.5}P_{0.5} quantum dots embedded in InP nanowires with radius $R=10$ nm follow the same trends as pure InAs insertions, with a crossover between perpendicular and parallel polarizations still around $t_{\text{InAs}}=8$ nm. Although alloying breaks the symmetry of the nanowire, it does not, therefore, significantly mix the highest-lying $E_{1/2}$ and $E_{3/2}$ hole states. The parallel and perpendicular oscillator strengths are, however, reduced by almost $\approx 30\%$.

To gain further insight into the optical properties of the NWHETs, the parallel and perpendicular oscillator strengths of InAs/InP nanowires with radius $R=10$ nm are plotted as a function of energy in Fig. 8 ($t_{\text{InAs}}=4$ nm) and Fig. 9 ($t_{\text{InAs}}=16$ nm). They are roughly proportional to the absorption (up to a $1/E$ factor). In the 4 nm thick layers, the f_{\perp} spectrum is dominated by the E1H1 transition at $E=0.747$ eV

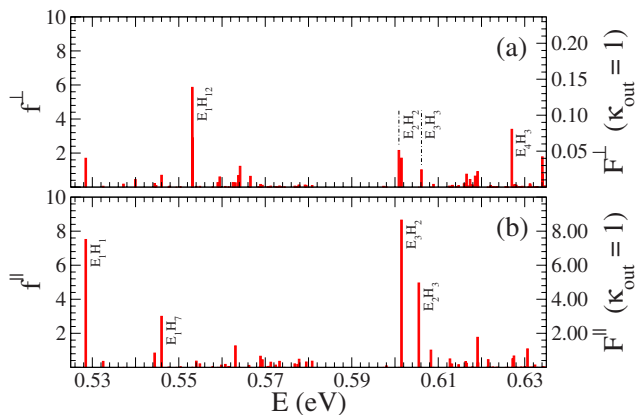


FIG. 9. (Color online) Oscillator strength spectrum (parallel and perpendicular polarizations) of InAs/InP nanowire heterostructures with $R=10$ nm and $t_{\text{InAs}}=16$ nm.

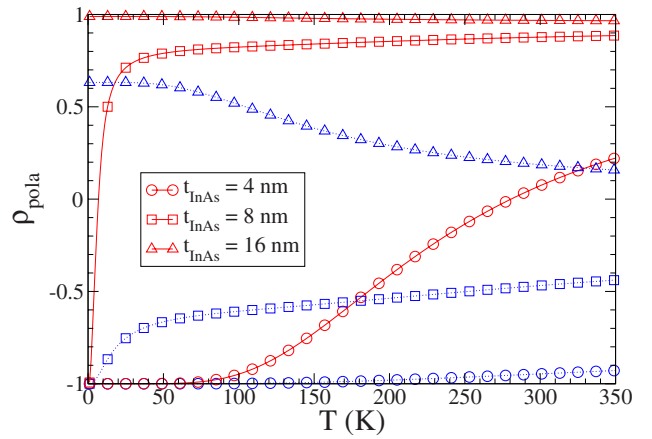


FIG. 10. (Color online) Polarization ratio as a function of the temperature T for InAs/InP nanowire heterostructures with $R=10$ nm and $t_{\text{InAs}}=4, 8,$ and 16 nm, with [solid (red) line] and without [dotted (blue) line] local-field effects.

and by the E2H3 and E3H2 transitions at much higher energy ($E>0.81$ eV). There is no oscillator strength at low energy in the f_{\parallel} spectrum, except for a deep hole transition (E1H7) around $E=0.792$ eV. We might therefore expect a robust perpendicular polarization at low temperatures. The spectrum of the 16 nm thick layers is somewhat richer. As discussed earlier, the E1H1 transition ($E=0.528$ eV) is now mostly polarized along the axis of the nanowire, while the perpendicular-polarized transitions have sunk deep into the valence band [$E(\text{E1H12})=0.553$ eV]. Like the E1H1 transition, the bright E2H3 and E3H2 transitions are mostly polarized along z .

The linear polarization ratio ρ_{pola} is finally plotted as a function of the temperature T in Fig. 10, for three different InAs/InP NWHETs, with and without ($K_{\perp}=1$) LFEs. In the latter case, the light is, as expected, polarized perpendicular to the nanowire in thin InAs layers ($t_{\text{InAs}}=4$ nm) up to room temperature. Local-field effects, however, almost kill the perpendicular oscillator strength, which results in a smooth decrease of ρ_{pola} as the H7 and E3 levels get occupied (and in a strong reduction of the intensity). In the 16 nm thick layers, the linear polarization ratio is close to 0.6 at low temperature (without LFEs), as expected for a light-hole-like E1H1 transition (see above discussion). The emission is, however, almost completely polarized along z once local-field effects are taken into account. The 8 nm thick layers provide an interesting intermediate case around the $E_{3/2}$ to $E_{1/2}$ symmetry crossover: The E1H1 transition is still polarized perpendicular to the nanowire,⁷² but lies very close (<2 meV) to a fairly bright E1H3 transition polarized along z . Therefore, the linear polarization ratio decreases much faster with T than in the 4 nm thick layers. The light is indeed strongly polarized along the nanowire above 20 K once LFEs are included. This clearly identifies the local-field effects as the main source of polarization anisotropy in InAs/InP NWHETs, as already evidenced for homogeneous InP nanowires.^{67–69}

IV. InP BARRIERS IN InAs NANOWIRES

In this section, we discuss the properties of InP and InAsP barriers embedded in InAs nanowires. Their height indeed determines the tunneling and thermionic currents through, e.g., nanowire resonant tunneling diodes,²² or the retention time of nanowire memories.^{27,28} The actual shape of these barriers depends on the piezoelectric and self-consistent electronic potentials, hence on the bias voltage and details of the tunneling device (doping profile, etc.).³⁶ These potentials will be neglected in the present work, which focuses on the effect of strains on the height of In(As)P conduction band barriers.

The conduction band offset between bulk unstrained InAs and InP is $\Delta_c^{\text{bulk}} \approx 0.60$ eV.⁴⁵ In an InAs/InP heterostructure, the InP barriers are put under tensile strain by the InAs layers, which tends to lower the conduction band energy E_c . The first-order shift δE_c is actually proportional to the hydrostatic strain,^{45,74}

$$\delta E_c = a_c(\varepsilon_{xx} + \varepsilon_{yy} + \varepsilon_{zz}), \quad (8)$$

where $a_c = -5.2$ eV is the conduction band deformation potential of InP. In an InAs/InP planar [two dimensional (2D)] heterostructure biaxially strained to InAs ($\varepsilon_{xx} = \varepsilon_{yy} = \varepsilon_{\parallel} = 3.23\%$, $\varepsilon_{zz} = \varepsilon_{\perp} = -2.04\%$), the conduction band barrier height would therefore be

$$\Delta_c^{2D} = \Delta_c^{\text{bulk}} + a_c(2\varepsilon_{\parallel} + \varepsilon_{\perp}) = 0.38 \text{ eV}. \quad (9)$$

The tight-binding model, which includes nonlinear effects beyond Eq. (8), yields $\Delta_c^{2D} = 0.40$ eV. This is significantly smaller than the unstrained band offset Δ_c^{bulk} .

The conduction band barrier height in InAs/InP NWHETs is expected to range between the 2D ($\Delta_c^{2D} = 0.4$ eV) and bulk ($\Delta_c^{\text{bulk}} = 0.6$ eV) limits. The strains are, however, much more inhomogeneous in nanowire heterostructures, especially in thin InP layers (the situation being symmetric to the one discussed in Sec. III A). As an illustration, the local conduction band energy $E_c(\mathbf{r})$ in an InAs/InP NWHET with $R = 10$ nm and $t_{\text{InP}} = 4$ nm is plotted in Fig. 11. $E_c(\mathbf{r})$ has been computed as the TB conduction band energy of the underlying bulk material with the same strains as in the nanowire. It is measured with respect to the conduction band edge of bulk unstrained InAs and, therefore, tends to zero far away from the InP layer. The latter is almost completely relaxed at the surface of the nanowire but is still significantly dilated deeper inside. As a consequence, the barrier is lower along the axis of the nanowire than at its surface. In thick InP layers, which are almost free of strains, the conduction band energy is close to the unstrained value $E_c(\mathbf{r}) \approx 0.6$ eV everywhere except around the interfaces.

To get a better understanding of tunneling in NWHETs, we can define an effective one-dimensional potential profile $V_c(z)$ in the spirit of the effective mass approximation.⁶¹ Let $\varepsilon_c(k_z)$ and $\Psi_{c,k_z}(\mathbf{r}) = e^{ik_z z} u_{c,k_z}(\mathbf{r})$ be the confinement energy and wave function for the lowest conduction subband of a *homogeneous* InAs or InP nanowire, where k_z is the longitudinal wave vector and $u_{c,k_z}(\mathbf{r})$ is periodic along the nanowire. The subband minimum at $k_z = 0$ can be characterized by its effective mass $m^*(R)$,

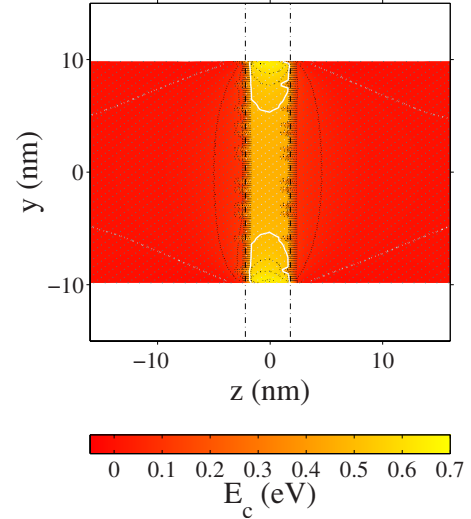


FIG. 11. (Color online) Conduction band energy $E_c(\mathbf{r})$ in an InAs/InP nanowire heterostructure with $R = 10$ nm and $t_{\text{InP}} = 4$ nm. E_c is measured with respect to the conduction band edge of bulk unstrained InAs. The dots are the As/P atoms in the (yz) plane of the plot. The vertical dash-dotted lines delimit the InP layer. The spacing between isolevel curves is 50 meV, the white dashed line being $E_c = 0$ and the white solid line $E_c = 0.5$ eV.

$$\varepsilon_c(k_z) \sim \varepsilon_c^0(R) + \frac{\hbar^2 k_z^2}{2m^*(R)}. \quad (10)$$

Analytical expressions for the confinement energy $\varepsilon_c^0(R)$ and effective mass $m^*(R)$ in InAs and InP nanowires have been given⁷⁵ in Ref. 47. Neglecting intersubband couplings in an effective mass-like approximation, the wave functions of the NWHET can be written $\Psi(\mathbf{r}) = \varphi(z)u_{c,0}(\mathbf{r})$, where the envelope function $\varphi(z)$ satisfies the equation

$$-\frac{d}{dz} \frac{\hbar^2}{2m^*(z)} \frac{d}{dz} \varphi(z) + [\varepsilon_c^0(z) + \Delta(z) + \delta V_c(z)] \varphi(z) = \varepsilon \varphi(z). \quad (11)$$

$\varepsilon_c^0(z)$ and $m^*(z)$ are the conduction band edge energy and effective mass of a homogeneous InAs or InP nanowire, $\Delta(z) = 0$ in InAs and $\Delta(z) = \Delta_c^{\text{bulk}}$ in InP are the unstrained conduction band profile in the heterostructure, and $\delta V_c(z) \sim \langle u_{c,0} | \delta E_c(\mathbf{r}) | u_{c,0} \rangle$ is the strain potential, the expectation value of $\delta E_c(\mathbf{r})$ being computed in a unit cell centered around z . Intersubband couplings (that would mix $u_{c,0}$ with higher-lying modes) are expected to be small for energies ε close to the conduction band edge of the InAs nanowire.

The effective potential $V_c(z) = \varepsilon_c^0(z) + \Delta(z) + \delta V_c(z)$ is plotted in Fig. 12 for InAs/InP NWHETs with radius $R = 10$ nm and various t_{InP} . The reference of energies is the conduction band edge $\varepsilon_{c,\text{InAs}}^0(R)$ of a homogeneous InAs nanowire, so that $V_c(z) \rightarrow 0$ when $z \rightarrow \pm \infty$. As expected, the barrier height is close to the 2D limit (0.4 eV) in thin layers and tends to (but does not reach) the bulk value (0.6 eV) in thick ones. The barrier is, moreover, rounded by strain relaxation around the interfaces. There is, interestingly, a small

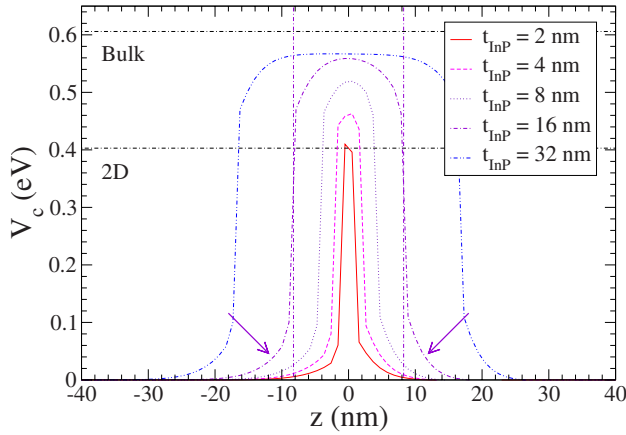


FIG. 12. (Color online) Effective potential $V_c(z)$ in an InAs/InP NWHET with radius $R=10$ nm. The bulk and 2D barrier heights are reported in the figure. The vertical dotted lines delimit the 16 nm thick InP layer, and the arrows point to the small barrier that appears on each side in InAs.

barrier on the InAs side of the interfaces due to the transfer of (compressive) strains from the InP layer (arrows in Fig. 12). This additional barrier might hinder the transport of low-energy electrons at small bias in tunneling devices.

As pointed out before, $V_c(z)$ never reaches the bulk limit in thick layers (and actually falls below the 2D limit in the thinnest ones). Indeed, lateral confinement rises the conduction band energy $\varepsilon_c^0(R)$ faster in InAs than in InP, which lowers the effective barrier. We might therefore split the barrier height Δ_c [computed as the maximum of $V_c(z)$] into two parts,

$$\Delta_c = [\varepsilon_{c,\text{InP}}^0(R) - \varepsilon_{c,\text{InAs}}^0(R)] + \Delta_c^{\text{str}}, \quad (12)$$

where Δ_c^{str} accounts for the strained band offset and is free of quantum confinement effects. The maximum barrier height is thus $\Delta_c^{\text{max}} = \varepsilon_{c,\text{InP}}^0(R) - \varepsilon_{c,\text{InAs}}^0(R) + \Delta_c^{\text{bulk}}$, i.e., about 0.57 eV for $R=10$ nm and about 0.59 eV for $R=20$ nm. This value lies in the experimental range (0.57–0.60 eV) deduced from the temperature dependence of the thermionic current through InAs/InP nanowire heterostructures.^{6,18,76}

Δ_c^{str} is finally plotted in Fig. 13 for InAs/InP NWHETs with different radii. Like ρ_{strains} , it shows a clear dependence on t_{InP}/R . It can therefore be fitted for $0 \leq t_{\text{InP}}/R \leq 3.5$ by

$$\frac{\Delta_c^{\text{str}}}{\Delta_c^{\text{bulk}}} = f(t_{\text{InP}}/R) = 1 - \frac{0.34}{1 + 0.92(t_{\text{InP}}/R) + 4.15(t_{\text{InP}}/R)^{2.41}}, \quad (13)$$

which is plotted as a dashed line in Fig. 13. The effects of the residual strains on the conduction band barrier are negligible when $t_{\text{InP}} \geq 1.5R$. However, most tunneling devices are in the $t_{\text{InP}} \ll R$ range where the height of the barrier can be reduced by $\approx 30\%$. This should be taken into account in the assessment and optimization of the performances of these devices.^{22,27,28}

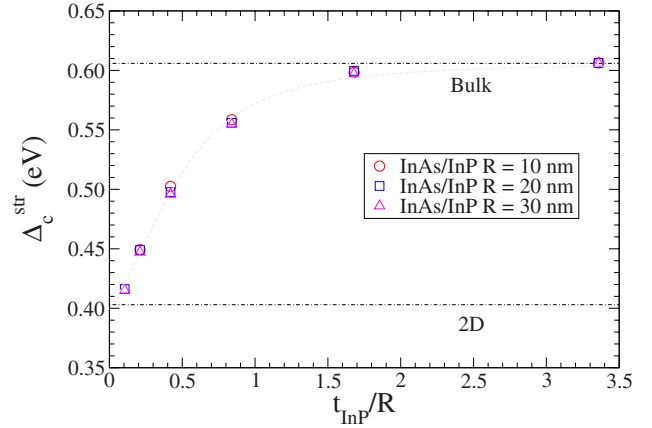


FIG. 13. (Color online) Conduction band barrier height Δ_c^{str} in InAs/InP nanowire heterostructures as a function of t_{InP}/R . The bulk and 2D barrier heights are reported in the figure. The dashed line is Eq. (13).

Alloying InP with InAs provides further control over the barrier height. Thin InP barriers might, moreover, be nonintentionally alloyed with the InAs nanowire. We have, therefore, also computed the conduction band height of $\text{InAs}_x\text{P}_{1-x}$ tunnel barriers embedded in InAs nanowires as a function of their thickness t_{InAsP} and as a function of the As mole fraction x . As evidenced in Fig. 14, Δ_c^{str} nicely scales with the conduction band offset $\Delta_c^{\text{bulk}}(x) \approx 0.6(1-x)$ eV between bulk, unstrained InAs and $\text{InAs}_x\text{P}_{1-x}$. As a matter of fact, the bowing parameters of the alloy are small,⁷⁷ and the conduction band deformation potentials a_c of InAs and InP are close enough to limit nonlinear effects,

$$\Delta_c^{\text{str}} \approx \Delta_c^{\text{bulk}}(x)f(t_{\text{InAsP}}/R), \quad (14)$$

where f is defined by Eq. (13). As discussed previously around Eq. (12), the actual barrier height Δ_c will be slightly lower than Δ_c^{str} due to the imbalance between lateral confine-

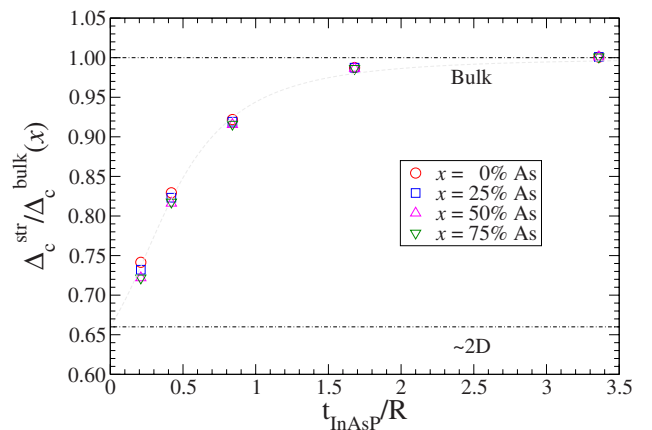


FIG. 14. (Color online) Normalized conduction band barrier height $\Delta_c^{\text{str}}/\Delta_c^{\text{bulk}}(x)$ in InAs/InAs_xP_{1-x} nanowire heterostructures as a function of t_{InAsP}/R for various As mole fractions x ($R=10$ nm). The bulk and 2D ($x=1$) barrier heights are reported in the figure. The dashed line is Eq. (13).

ment in the InAs and InAs_xP_{1-x} segments. A linear interpolation between the confinement energies of pure InAs and InP nanowires,^{47,75} $\Delta_c \approx (1-x)[\varepsilon_{c,\text{InP}}^0(R) - \varepsilon_{c,\text{InAs}}^0(R)] + \Delta_c^{\text{str}}$, though crude, is nonetheless a reasonable approximation in the $R \gtrsim 10$ nm range.

V. CONCLUSION

We have investigated the electronic and optical properties of InAs quantum dots embedded in InP nanowires, as well as the height of InP tunnel barriers in InAs nanowires. We have shown that the residual strains did not trap the electrons and holes as in the highly mismatched InAs/GaAs nanowire heterostructures,^{30,31} though the piezoelectric potential still tends to separate the electrons and holes in thick InAs layers. The InAs quantum dots, therefore, exhibit bright optical transitions. The absorption and luminescence are polarized perpendicular to the wire in thin InAs layers and parallel to the wire in thick ones. This rotation results from the increasing light-hole character of the exciton. Indeed, the ground-state hole wave function has a clear heavy-hole character in thin, quantum-well-like InAs layers, but gets lighter with increasing thickness as lateral confinement by the nanowire overcomes longitudinal confinement by the heterostructure. The parallel polarization is also favored by the local-field effects

that arise from the dielectric mismatch between the nanowires and their surroundings. They indeed tend to reduce the perpendicular polarization with increasing temperature and lead to a giant and robust polarization anisotropy in thick InAs quantum dots. We point out that the effects of the piezoelectric fields should be much smaller in $\langle 001 \rangle$ -oriented^{6,22,78} than in $\langle 111 \rangle$ -oriented nanowires and that the effects of residual strains might be more sensitive in nanowire heterostructures with larger effective masses than InAs.

As for In(As)P tunnel barriers in InAs nanowires, we have shown that the residual strains can significantly decrease the conduction band barrier height. The latter indeed tends to the bulk limit (0.6 eV) in InP layers with thickness $t_{\text{InP}} \gtrsim 1.5R$, but is close to the 2D limit (0.4 eV) in the $t_{\text{InP}} \ll R$ range encountered in most nanowire tunneling devices. This reduction of the barrier height must therefore be taken into account in the design of these devices.

ACKNOWLEDGMENTS

This work was supported by the French “Action Concertée Incitative” (ACI) “TransNanofils” and by the European Integrated Project (IP) NODE (EU Contract No. 015783 NODE).

*yniquet@cea.fr

- ¹A. M. Morales and C. M. Lieber, *Science* **279**, 208 (1998).
- ²A. I. Persson, M. W. Larsson, S. Stenström, B. J. Ohlsson, L. Samuelson, and L. R. Wallenberg, *Nat. Mater.* **3**, 677 (2004).
- ³K. A. Dick, K. Deppert, T. Mårtensson, B. Mandl, L. Samuelson, and W. Seifert, *Nano Lett.* **5**, 761 (2005).
- ⁴W. Lu and C. M. Lieber, *J. Phys. D* **39**, R387 (2006).
- ⁵Y. Wu, R. Fan, and P. Yang, *Nano Lett.* **2**, 83 (2002).
- ⁶M. T. Björk, B. J. Ohlsson, T. Sass, A. I. Persson, C. Thelander, M. H. Magnusson, K. Deppert, L. R. Wallenberg, and L. Samuelson, *Appl. Phys. Lett.* **80**, 1058 (2002).
- ⁷M. S. Gudiksen, L. J. Lauhon, J. Wang, D. C. Smith, and C. M. Lieber, *Nature (London)* **415**, 617 (2002).
- ⁸L. J. Lauhon, M. S. Gudiksen, D. Wang, and C. M. Lieber, *Nature (London)* **420**, 57 (2002).
- ⁹F. Glas, *Phys. Rev. B* **74**, 121302(R) (2006).
- ¹⁰S. Raychaudhuri and E. T. Yu, *J. Appl. Phys.* **99**, 114308 (2006).
- ¹¹M. W. Larsson, J. B. Wagner, M. Wallin, P. Håkansson, L. E. Fröberg, L. Samuelson, and L. R. Wallenberg, *Nanotechnology* **18**, 015504 (2007).
- ¹²J. Xiang, W. Lu, Y. Hu, Y. Wu, H. Yan, and C. M. Lieber, *Nature (London)* **441**, 489 (2006).
- ¹³M. Hanke, C. Eisenschmidt, P. Werner, N. D. Zakharov, F. Syrovatka, F. Heyroth, P. Schäfer, and O. Kononov, *Phys. Rev. B* **75**, 161303(R) (2007).
- ¹⁴M. T. Borgström, V. Zwiller, E. Müller, and A. Imamoglu, *Nano Lett.* **5**, 1439 (2005).
- ¹⁵J. Noborisaka, J. Motohisa, S. Hara, and T. Fukui, *Appl. Phys. Lett.* **87**, 093109 (2005).
- ¹⁶F. Qian, S. Gradečak, Y. Li, C.-Y. Wen, and C. M. Lieber, *Nano Lett.* **5**, 2287 (2005).
- ¹⁷C. Thelander, P. Agarwal, S. Brongersma, J. Eymery, L. F. Feiner, A. Forchel, M. Scheffler, W. Riess, B. J. Ohlsson, U. Gösele, and L. Samuelson, *Mater. Today* **9**, 28 (2006).
- ¹⁸M. T. Björk, B. J. Ohlsson, T. Sass, A. I. Persson, C. Thelander, M. H. Magnusson, K. Deppert, L. R. Wallenberg, and L. Samuelson, *Nano Lett.* **2**, 87 (2002).
- ¹⁹A. I. Persson, M. T. Björk, S. Jeppesen, J. B. Wagner, L. R. Wallenberg, and L. Samuelson, *Nano Lett.* **6**, 403 (2006).
- ²⁰P. Mohan, J. Motohisa, and T. Fukui, *Appl. Phys. Lett.* **88**, 133105 (2006).
- ²¹M. Tchernycheva, G. E. Cirlin, G. Patriarche, L. Travers, V. Zwiller, U. Perinetti, and J. C. Harmand, *Nano Lett.* **7**, 1500 (2007).
- ²²M. T. Björk, B. J. Ohlsson, C. Thelander, A. I. Persson, K. Deppert, L. R. Wallenberg, and L. Samuelson, *Appl. Phys. Lett.* **81**, 4458 (2002).
- ²³E. Lind, A. I. Persson, L. Samuelson, and L.-E. Wernersson, *Nano Lett.* **6**, 1842 (2006).
- ²⁴C. Thelander, T. Martenson, M. T. Björk, B. J. Ohlsson, M. W. Larsson, L. R. Wallenberg, and L. Samuelson, *Appl. Phys. Lett.* **83**, 2052 (2003).
- ²⁵M. T. Björk, A. Fuhrer, A. E. Hansen, M. W. Larsson, L. E. Fröberg, and L. Samuelson, *Phys. Rev. B* **72**, 201307(R) (2005).
- ²⁶A. Fuhrer, L. E. Fröberg, J. N. Pedersen, M. W. Larsson, A. Wacker, M.-E. Pistol, and L. Samuelson, *Nano Lett.* **7**, 243 (2007).
- ²⁷C. Thelander, H. A. Nilsson, L. E. Jensen, and L. Samuelson, *Nano Lett.* **5**, 635 (2005).
- ²⁸H. A. Nilsson, C. Thelander, L. E. Fröberg, J. B. Wagner, and L.

Samuelson, Appl. Phys. Lett. **89**, 163101 (2006).

²⁹E. D. Minot, F. Kelkensberg, M. van Kouwen, J. A. van Dam, L. P. Kouwenhoven, V. Zwiller, M. T. Borgström, O. Wunnicke, M. A. Verheijen, and E. P. A. M. Bakkers, Nano Lett. **7**, 367 (2007).

³⁰Y. M. Niquet, Phys. Rev. B **74**, 155304 (2006).

³¹Y. M. Niquet, Nano Lett. **7**, 1105 (2007).

³²M. P. Persson and H. Q. Xu, Phys. Rev. B **73**, 035328 (2006).

³³C. Simon, Y. M. Niquet, X. Caillet, J. Eymery, J.-P. Poizat, and J.-M. Gérard, Phys. Rev. B **75**, 081302(R) (2007).

³⁴B. J. Ohlsson, M. T. Björk, A. I. Persson, C. Thelander, L. R. Wallenberg, M. H. Magnusson, K. Deppert, and L. Samuelson, Physica E (Amsterdam) **13**, 1126 (2002).

³⁵N. Panev, A. I. Persson, N. Sköld, and L. Samuelson, Appl. Phys. Lett. **83**, 2238 (2003).

³⁶M. Zervos and L. F. Feiner, J. Appl. Phys. **95**, 281 (2004).

³⁷P. N. Keating, Phys. Rev. **145**, 637 (1966).

³⁸The bond-stretching and bond-bending constants of InP are, respectively, $\alpha=39.82$ N/m and $\beta=8.13$ N/m. The VFF elastic constants of InP are therefore $c_{11}=109.4$ GPa, $c_{12}=54.0$ GPa, and $c_{44}=46.0$ GPa, while the experimental (Ref. 39) elastic constants are $c_{11}=102.2$ GPa, $c_{12}=57.6$ GPa, and $c_{44}=46.0$ GPa. The elastic constants of InAs are given in Ref. 30.

³⁹*Physics of Group IV Elements and III-V Compounds*, Landolt-Börnstein, New Series, Group III, Vol. 17, Pt. A, edited by O. Madelung, M. Schulz, and H. Weiss (Springer-Verlag, New York, 1982).

⁴⁰S. Salon and M. V. K. Chari, *Numerical Methods in Electromagnetism* (Academic, San Diego, 1999).

⁴¹J. C. Slater and G. F. Koster, Phys. Rev. **94**, 1498 (1954).

⁴²A. Di Carlo, Semicond. Sci. Technol. **18**, R1 (2003).

⁴³C. Delerue and M. Lannoo, *Nanostructures: Theory and Modeling* (Springer, New York, 2004).

⁴⁴J.-M. Jancu, R. Scholz, F. Beltram, and F. Bassani, Phys. Rev. B **57**, 6493 (1998).

⁴⁵C. G. Van de Walle, Phys. Rev. B **39**, 1871 (1989).

⁴⁶The TB deformation potentials of InP are $a_v=1.27$ eV, $a_c=-5.20$ eV, $b=-1.6$ eV, and $d=-4.2$ eV, in agreement with the *ab initio* calculations of Ref. 45. Those of InAs are given in Ref. 30. The valence band offset between InAs and InP is $\Delta_v^{\text{bulk}}=0.4$ eV, consistent with the measurements of Refs. 6 and 18.

⁴⁷Y. M. Niquet, A. Lherbier, N. H. Quang, M. V. Fernández-Serra, X. Blase, and C. Delerue, Phys. Rev. B **73**, 165319 (2006).

⁴⁸The static ($\kappa_{\text{in}}^0=15$) and optical ($\kappa_{\text{in}}^\infty=12$) dielectric constants of the nanowire are the same as in Ref. 30.

⁴⁹G. L. G. Sleijpen and H. A. Van der Vorst, SIAM J. Matrix Anal. Appl. **17**, 401 (1996); SIAM Rev. **42**, 267 (2000).

⁵⁰ $(\Delta\Omega/\Omega_0)_{\text{QW}}=2\varepsilon_{\parallel}+\varepsilon_{zz}$, with $\varepsilon_{zz}=1.755\%$ in $\langle 111 \rangle$ -oriented InAs/InP QWs biaxially strained on InP.

⁵¹Y. M. Niquet, C. Priester, and H. Mariette, Phys. Rev. B **55**, R7387 (1997).

⁵²This follows from the scaling properties of linear elasticity: In the limit $L \rightarrow \infty$, the strains $\varepsilon_{ij}(x, y, z)$ in a nanowire with characteristic dimensions αR and αt_{InAs} are, indeed, equal to the strains $\varepsilon_{ij}(x/\alpha, y/\alpha, z/\alpha)$ in a nanowire with characteristic dimensions R and t_{InAs} . Therefore, the average hydrostatic strain and ρ_{strain} only depend on t_{InAs}/R .

⁵³The legend in Fig. 1 of Ref. 30 should read $R=8$ nm (instead of $R=16$ nm) and $R=10$ nm (instead of $R=20$ nm). The figure itself is, however, correct.

⁵⁴J. D. Jackson, *Classical Electrodynamics* (Wiley, New York,

1975).

⁵⁵For consistency, the results given for InAs/GaAs NWHTs do not take into account the second-order piezoelectric effects (Ref. 56) discussed in Ref. 31.

⁵⁶G. Bester, X. Wu, D. Vanderbilt, and A. Zunger, Phys. Rev. Lett. **96**, 187602 (2006).

⁵⁷The wave functions were plotted with v_{SIM}, a free 3D visualization tool available at: http://www-drfrm.ccea.fr/sp2m/L_Sim/V_Sim

⁵⁸The wave functions E2/E3, E4/E5 ($t_{\text{InAs}}=4$ nm), and E5/E6 ($t_{\text{InAs}}=16$ nm) have been recomputed without spin-orbit coupling for Fig. 4, in order to better display their spatial symmetries.

⁵⁹The tight-binding wave functions $\Psi(\mathbf{r})$ can, indeed, be analyzed in an envelope-function framework (Ref. 61) and expanded as

$$\Psi(\mathbf{r}) = f_{-3/2}(\mathbf{r})u_{-3/2}(\mathbf{r}) + f_{+3/2}(\mathbf{r})u_{+3/2}(\mathbf{r}) + f_{-1/2}(\mathbf{r})u_{-1/2}(\mathbf{r}) + f_{+1/2}(\mathbf{r})u_{+1/2}(\mathbf{r}) + \Psi_r(\mathbf{r}),$$

where $u_{m_j}(\mathbf{r})$ is the $|\frac{3}{2}, m_j\rangle$ bulk valence band wave function at $\mathbf{k}=0$, $f_{m_j}(\mathbf{r})$ is the associated envelope function in the nanowire, and $\Psi_r(\mathbf{r})$ is the remainder (contributions from the other bands and hydrogen atoms). The $|\frac{3}{2}, \pm\frac{3}{2}\rangle$ Bloch functions describe heavy holes along the quantization axis $z=[111]$, while the $|\frac{3}{2}, \pm\frac{1}{2}\rangle$ describe light holes. The heavy- and light-hole contributions given in Table II are the total weights of the $|\frac{3}{2}, \pm\frac{3}{2}\rangle$ and $|\frac{3}{2}, \pm\frac{1}{2}\rangle$ envelopes, respectively.

⁶⁰D. L. Smith and C. Mailhot, Rev. Mod. Phys. **62**, 173 (1990).

⁶¹G. Bastard, *Wave Mechanics Applied to Semiconductor Heterostructures* (Les Editions de Physique, Les Ulis, 1988).

⁶²Z. Zanolli, F. Fuchs, J. Furthmüller, U. von Barth, and F. Bechstedt, Phys. Rev. B **75**, 245121 (2007).

⁶³F. Glas, J.-C. Harmand, and G. Patriarche, Phys. Rev. Lett. **99**, 146101 (2007).

⁶⁴F. M. Peeters, A. Matulis, M. Helm, T. Fromherz, and W. Hilber, Phys. Rev. B **48**, 12008 (1993).

⁶⁵For light incident or emitted perpendicular to the nanowire, with the electric field making an angle θ with the z axis, $f_{ij}(\mathbf{e}) \equiv f_{ij}(\theta) = f_{ij}^{\parallel} \cos^2 \theta + f_{ij}^{\perp} \sin^2 \theta$. The effective oscillator strength F_{ij} and recombination rate $\langle \omega \rangle$ follow the same angular dependence.

⁶⁶E. A. Muljarov, E. A. Zhukov, V. S. Dneprovskii, and Y. Masumoto, Phys. Rev. B **62**, 7420 (2000).

⁶⁷J. Wang, M. S. Gudiksen, X. Duan, Y. Cui, and C. M. Lieber, Science **293**, 1455 (2001).

⁶⁸M. P. Persson and H. Q. Xu, Phys. Rev. B **70**, 161310(R) (2004).

⁶⁹M. Califano and A. Zunger, Phys. Rev. B **70**, 165317 (2004).

⁷⁰G. Allan, C. Delerue, and Y. M. Niquet, Phys. Rev. B **63**, 205301 (2001).

⁷¹M. Graf and P. Vogl, Phys. Rev. B **51**, 4940 (1995).

⁷²According to Fig. 3(b), the perpendicular polarization should already be allowed at $t_{\text{InAs}}=8$ nm because the single-particle H1 state has the $E_{1/2}$ symmetry. However, the nearby $E_{3/2}$ state remains the actual ground state once the electron-hole interaction is taken into account.

⁷³The heavy-hole envelopes (Ref. 58) of the H1 wave function, $f_{\pm 3/2}(\mathbf{r})$, are indeed orthogonal to the conduction band envelope of the E1 wave function in the $E_{1/2}$ symmetry.

⁷⁴G. L. Bir and G. E. Pikus, *Symmetry and Strain-Induced Effects in Semiconductors* (Wiley, New York, 1974).

⁷⁵As a reminder, $\varepsilon_{c,\text{InAs}}^0(R) = 10.6951/(R^2 + 6.512R + 2.773)$ eV and $\varepsilon_{c,\text{InP}}^0(R) = 3.0696/(R^2 + 1.798R + 1.214)$ eV (R in nanometers).

⁷⁶Although the nanowires of Ref. 22 are $\langle 001 \rangle$ oriented, the conduction band edge energies $\varepsilon_c^0(R)$ (hence, the maximum barrier height) are equivalent to those of $\langle 111 \rangle$ -oriented nanowires, as shown in Ref. 47.

⁷⁷M. Wada, S. Araki, T. Kudou, T. Umezawa, S. Nakajima, and T. Ueda, *Appl. Phys. Lett.* **76**, 2722 (2000).

⁷⁸U. Krishnamachari, M. Borgström, B. J. Ohlsson, N. Panev, L. Samuelson, W. Seifert, M. W. Larsson, and L. R. Wallenberg, *Appl. Phys. Lett.* **85**, 2077 (2004).